batteries

MDPI

Article

Ni_3S_2@NiMo-LDH Composite for Flexible Hybrid Capacitors

Qi He and Xiang Wu *

School of Materials Science and Engineering, Shenyang University of Technology, Shenyang 110870, China
* Correspondence: wuxiang05@sut.edu.cn or wuxiang05@163.com

Abstract: Ni_3S_2 is a kind of transition metal sulfide (TMD) with excellent electrical conductivity and electrochemical activity. To further enhance the specific capacity of Ni_3S_2-based supercapacitors, we synthesize several nanosheet-decorated Ni_3S_2@NiMo-LDH nanostructures by a combination of hydrothermal and electrodeposition processes. The mesoporous structure provides a large number of electroactive sites, which shortens the charge transfer distance and increases the specific surface area of electrode materials. The assembled asymmetric supercapacitor shows an energy density of 62.8 W h kg^{-1} at 2701.6 W kg^{-1} and long-term cycling stability.

Keywords: supercapacitors; Ni_3S_2; layered double hydroxide; energy density

check for updates

Citation: He, Q.; Wu, X. Ni_3S_2@NiMo-LDH Composite for Flexible Hybrid Capacitors. *Batteries* **2024**, *10*, 230. https://doi.org/10.3390/batteries10070230

Academic Editor: Johan E. ten Elshof

Received: 25 May 2024
Revised: 17 June 2024
Accepted: 25 June 2024
Published: 26 June 2024

1. Introduction

With the growing global shortage of energy sources, it is imperative to develop some renewable materials for energy storage and conversion systems [1–5]. Therefore, supercapacitors are regarded as suitable candidates in energy storage fields because of their excellent electrochemical performance, environmental friendliness, and safety [6–8]. However, the low theoretical capacity remains a significant barrier to its practical application. One of the main components of the supercapacitor, electrode materials, is critical for improving the total electrochemical performance. Thus, it is necessary to design some emerging materials with superior performance [9–12].

Transition metal sulfides (Ni_3S_2, Co_9S_8, MoS_2, WS_2, and SnS_2) have attracted extensive attention because they possess higher electrochemical activity than metal oxides [13–16]. However, they present small, specific surface areas and poor cycling stability [17–19]. Moreover, due to their multiple redox reactions, layered double hydroxides (LDHs) show a large specific surface area [20–22]. However, their performance is still hampered by their low structural stability and poor dielectric properties [23,24]. The combination of Ni_3S_2 and NiMo-LDH structures might provide abundant electrochemical active sites and protect the active material from clumping or collapsing during charging and discharging. To the best of our knowledge, there are no reports about Ni_3S_2@NiMo-LDH electrode materials for electrochemical capacitors. The synthesis of Ni_3S_2@NiMo-LDH composites does not need to calcinate, which reduces the complexity of the process and the cost of production in mass production.

In this work, we prepare Ni_3S_2 microspheres by a facile hydrothermal route. Then, the NiMo-LDH nanosheets are coated on Ni_3S_2 samples by electrodeposition to obtain porous structures. The synthesized Ni_3S_2@NiMo-LDH-150 electrode material delivers a capacitance of 1940 F g^{-1} at 1 A g^{-1} and a capacity of 77% after 10,000 cycles. At the same time, the as-fabricated ASC device provides an energy density of 63.7 W h kg^{-1} at 2708 W kg^{-1}. It has been found that the effect of repeated bending at various angles is negligible on capacitance. The capacitance hardly decreases at low temperatures after 2000 times of charging and discharging.

2. Experimental Section

2.1. Materials

All chemicals were analytical grade and used as purchased. The NF was purchased from Kunshan Guangjia New Material Co., Ltd. (Nantong, China). $Ni(NO_3)_2 \cdot 6H_2O$ and thiourea were obtained from Shanghai Aladdin Biochemical Technology Co. (Shanghai, China). $Na_2MoO_4 \cdot 2H_2O$ was obtained from Tianjin Damao Chemical Reagent Factory (Tianjin, China). Activated carbon (AC), polyvinylidene fluoride (PVDF), acetylene black, and N-methylpyrrolidone (NMP) were acquired from Taiyuan Lizhiyuan Technology Co., Ltd. (Taiyuan, China). Because of the experimental process, we need to sulfide the electrode material. Therefore, it was necessary to wear a protective mask throughout the process and carry out the process in a hood. The waste liquid generated was poured into a waste liquid bucket for disposal.

2.2. Synthesis of Ni_3S_2 Samples

A piece of NF (4 × 4 cm^2) was immersed in a 1 M HCl solution for 30 min. The NF was then repeatedly cleaned using deionized (DI) water and ethanol while being sonicated, and it was dried in an oven at 60 °C for 24 h. In a typical process, 3 mM of thiourea were dissolved in sequence in 30 mL of ethanol and stirred for 30 min. Then, the pretreated NF was placed into an autoclave and heated to 160 °C for 6 h. The as-prepared samples were gradually cooled to room temperature and then washed with deionized water and ethanol. Afterward, the precursors were dried at 60 °C under vacuum conditions for 8 h. The mass loading of active materials is 1.8 mg cm^{-2}.

2.3. Preparation of Ni_3S_2@NiMo-LDH Composite

NiMo-LDH nanosheets were grown on Ni_3S_2 samples. In detail, the Ni_3S_2 samples were immersed into an electrolyte containing 0.1 mol/L $Na_2(MoO_4)_2 \cdot 2H_2O$ and 0.1 mol/L $Ni(NO_3)_2 \cdot 6H_2O$ for 100 s, 150 s, and 200 s, respectively, at a potential of 0.9 V. The as-fabricated samples were named Ni_3S_2@NiMo-LDH-100, Ni_3S_2@NiMo-LDH-150, and Ni_3S_2@NiMo-LDH-200, with average mass loadings of 2, 2, and 2.2 mg cm^{-2}, respectively. A single NiMo-LDH sample was also synthesized for comparison.

2.4. Preparation of Activated Carbon Anode Material

In an onyx mortar, AC, acetylene black, and PVDF were combined in a 7:2:1 ratio. Ethanol was then incorporated into the mixture. Before the following grinding, the ethanol in the agate mortar was fully ground and evaporated each time. The NMP solution was dropped into the agate mortar and ground thoroughly after the third time. Using a spatula, the obtained slurry was spread evenly over the pretreated NF. It was then dried at 60 °C for 10 h.

2.5. Preparation of PVA-KOH Gel Electrolyte

Throughout the preparation, slow and uniform magnetic stirring was used to keep the hydrogels from clumping and agglomerating. First, a beaker filled with 20 milliliters of deionized water was submerged in a water bath. Then, 2 g of PVA were carefully added to the beaker once it reached a temperature of 60 °C. The 1.5 M KOH solution was gradually added to the PVA hydrogel in the water bath once the beaker reached a temperature of 90 °C. Finally, turn off the heat and let the gel cool to room temperature until the gel clarifies.

2.6. Structure Characterization

An X-ray diffraction analyzer (XRD, 7000, Shimadzu, Tokyo, Japan, λ = 0.1541 nm) over a coverage range of 10 to 90° was utilized to study the crystallographic structure of the as-synthesized samples. A scanning electron microscope (SEM, Gemini 300-71-31, Zeiss, Oberkochen, Germany) was conducted to characterize the morphology and structure. X-ray photoelectron spectra (XPS, ESCALAB250, Thermo Fischer, Waltham, MA, USA) were employed to investigate the element composition. N2 absorption and desorption

isotherms were used to perform their specific surface areas via a Brunauer-Emmett-Teller (BET, Micromeritics ASAP, Micromeritics, Norcross, GA, USA).

2.7. Electrochemical Characterization

The electrochemical characteristics of the samples were investigated in a three-electrode system. The electrodes were used directly as the working electrode, Hg/HgO as the reference electrode, and the Pt electrode as the counter electrode. The specific capacitance ($C\ g^{-1}$) of the electrodes was determined by the following equations [25]:

$$C = I\Delta\ t/m \tag{1}$$

where I is the discharge current (A), Δt refers to the discharge time (s), and m is the weight of active materials (g).

The electrochemical performance of a hybrid supercapacitor was studied in a two-electrode system. ASC was assembled with Ni_3S_2@NiMo-LDH-150 samples as positive materials, active carbon as negative ones, and PVA-KOH gel as an electrolyte. According to the principle of charge conservation ($Q^+ = Q^-$), the optimum mass ratio of negative to positive electrode material is controlled by the following equation [26]:

$$Q^+ = Q^- \tag{2}$$

$$Q = It = Cm\ \Delta V \tag{3}$$

where Q, I, t, C, m, and ΔV denote the charge storage capacity, discharge current (A), discharge time (s), specific capacitance ($C\ g^{-1}$), the mass of the materials (g), and the voltage window (V), respectively. The mass balance can be calculated according to equation [27]:

$$M^+/m^- = Cm^-(\Delta V)/Cm^+(\Delta V)^+ \tag{4}$$

C and ΔV are specific capacitance and voltage windows of the negative electrode materials.

The energy density (E) and power density (P) were calculated by the following equations:

$$E = 1/2CV^2 \tag{5}$$

$$P = 3600E/t \tag{6}$$

where E and P correspond to the energy density and power density of the device, respectively. V refers to the operating voltage. t represents the discharge time.

3. Results and Discussion

Figure 1 illustrates the growth process of the synthesized Ni_3S_2@NiMo-LDH samples. Firstly, Ni_3S_2 microspheres are uniformly grown on the nickel foam surface in a heating reaction. Then, a coating of NiMo-LDH nanosheets is formed on Ni_3S_2 microspheres by controllable electrodeposition.

Figure 2a first presents the XRD pattern of the as-obtained samples. The three strongest peaks at 43.5°, 51.6°, and 75.6° are related to the Ni phase (JCPDS No. 70-1849). The diffraction peaks at 21.2°, 30.46°, 37.04°, 49.3°, 54.52°, 68.52°, 72.36°, and 76.96° can be well indexed to the (101), (012), (003), (113), (300), (131), (214), and (401) planes of the Ni_3S_2 phase (JCPDS No. 08-0126), respectively. The diffraction peaks of Ni_3S_2 remained under the continuous coating of NiMo-LDH nanosheets. The peaks located at 34.8° and 59.4° diffraction can be assigned to the (012) and (110) planes of the NiMo-LDH phase (ICC card No. 01-082-8040) [28]. When the electrodeposition time is 100, 150, and 200 s, respectively, the XRD patterns of the materials show no significant change. The synthesis of Ni_3S_2@NiMo-LDH samples was demonstrated by the simultaneous discovery of characteristic peaks of two materials.

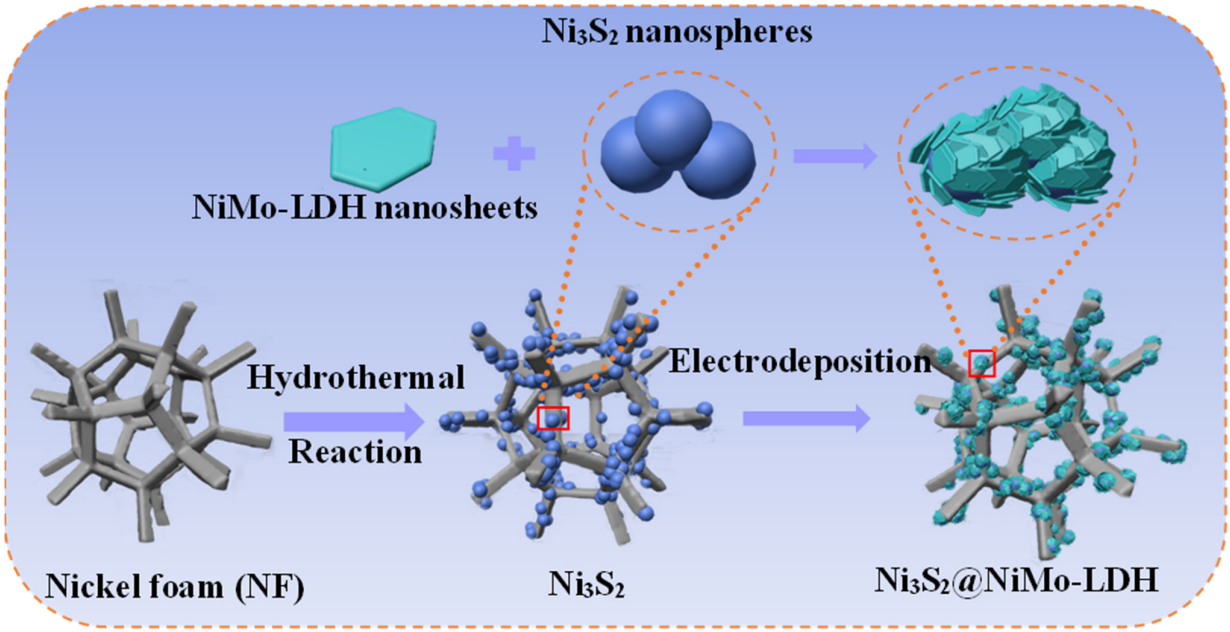

Figure 1. Preparation route schematic diagram of the Ni_3S_2@NiMo-LDH heterostructure.

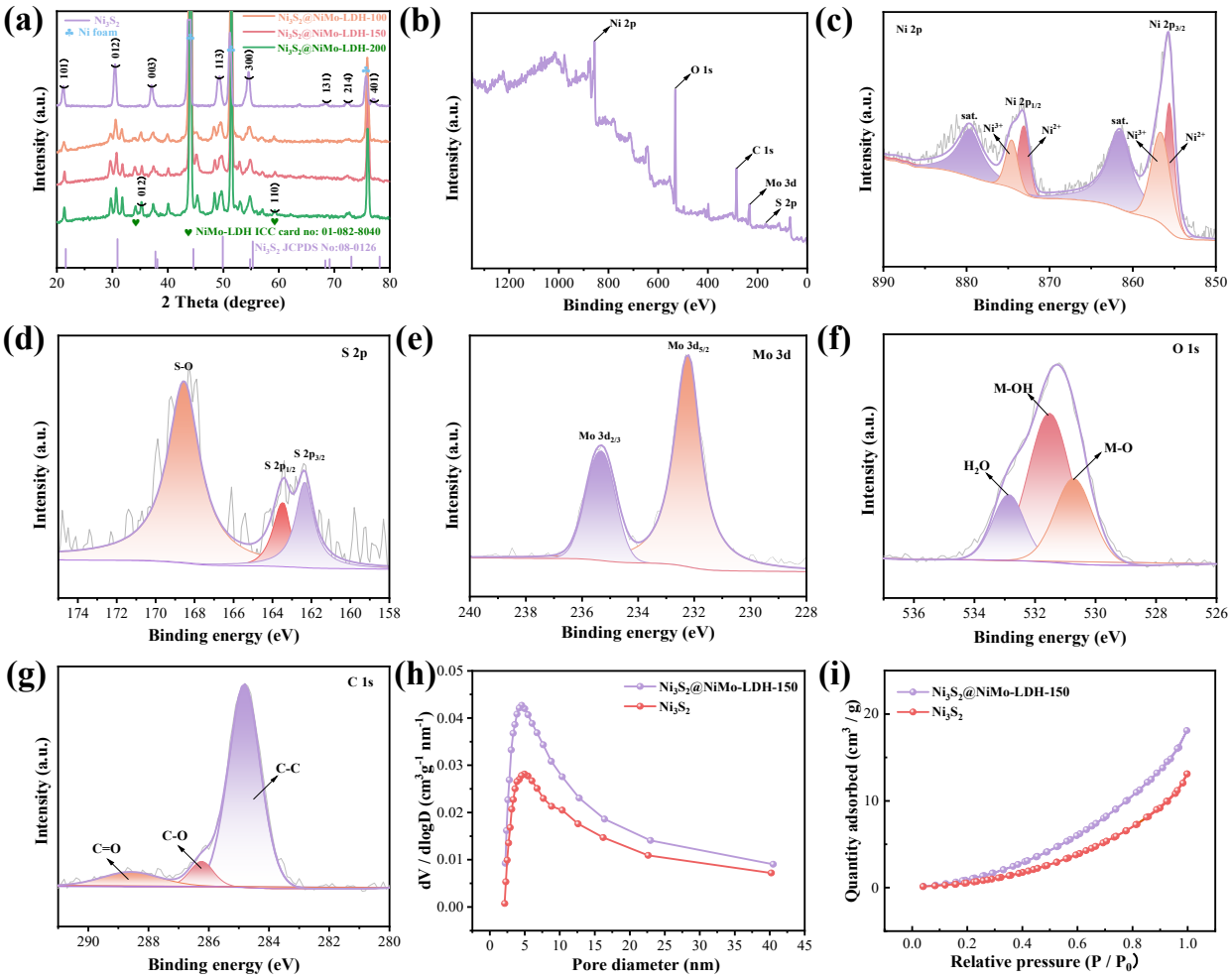

Figure 2. Structural characterization. (**a**) XRD patterns of Ni_3S_2 and Ni_3S_2@NiMo-LDH-150 samples; (**b**) XPS full spectra of Ni_3S_2@NiMo-LDH-150 sample; (**c**) Ni 2p; (**d**) S 2p; (**e**) Mo 3d; (**f**) O 1s; (**g**) C 1s; (**h**) pore size distributions; (**i**) N_2 adsorption/desorption isotherms.

Then, XPS is used to study the elemental valence distribution of the Ni_3S_2@NiMo-LDH-150 samples. In Figure 2b, the survey spectra confirm the presence of S, Ni, Mo, O, and C elements. In the Ni 2p spectra (Figure 2c), there are two spin-orbit double peaks (Ni $2p_{3/2}$ and Ni $2p_{1/2}$) at 855.7 and 873.4 eV and two satellite peaks (Ni 2p) at 879.6 and 861.6 eV, which are in accordance with Ni^{2+} and Ni^{3+} [29]. Figure 2d presents the XPS spectra of the S 2p orbit. The two peaks at 162.4 and 163.5 eV correspond to the S $2p_{3/2}$ and S $2p_{1/2}$ spin orbits, and another satellite peak at 168.6 eV is described as S $2p_{3/2}$, indicating the presence of S^{2-} [30]. From Figure 2e, two peaks at 235.3 and 232.2 eV are studied by fitting to the Mo $3d_{3/2}$ and Mo $3d_{5/2}$ spin orbits of Mo 3d, respectively [31]. Three distinct peaks are found in the O 1s region (Figure 2f) at 530.7, 531.5, and 532.8 eV. All of them are adsorbed water, hydroxyl groups (Mo-OH or Ni-OH), and metal-oxygen bonds (Mo-O or Ni-O) [32]. The C 1s spectrum (Figure 2g) is fitted to three signal peaks, including the C-C bond at 284.8 eV, the C-O bond at 286.2 eV, and the C=O bond at 288.6 eV [33]. The XPS study proves the presence of the Ni_3S_2@NiMo-LDH phase. Figure 2h,i show N_2 isotherms of Ni_3S_2 and Ni_3S_2@NiMo-LDH-150 samples. The typical type III isotherms demonstrate that the samples possess a mesoporous structure and a broad pore-size distribution. The BET surface area of the Ni_3S_2@NiMo-LDH-150 product is 37.654 $m^2\ g^{-1}$, which is larger than that of the Ni_3S_2 product (23.977 $m^2\ g^{-1}$). The total pore volumes of the Ni_3S_2@NiMo-LDH-150 and Ni_3S_2 samples are 0.027 and 0.019 $cm^3\ g^{-1}$, respectively. The results reveal that NiMo-LDH nanosheets capped with Ni_3S_2 microspheres increase the specific surface area and active sites.

After that, we research the morphologies and structures of the samples. Figure 3a,b show the SEM images of the Ni_3S_2 product. It shows interconnected microspheres with an average diameter of 300–500 nm. This microscopic morphology facilitates NiMo-LDH nanosheets being covered by the above materials. From Figure 3c,d, the SEM images of the Ni_3S_2@NiMo-LDH-150 product show that the Ni_3S_2 microspheres are evenly wrapped in NiMo-LDH nanosheets. These nanosheets possess an open surface structure, which is beneficial to the penetration of the electrolyte. The corresponding EDS plots indicate that the elements Ni, S, Mo, and O are present and continuously distributed throughout the surface of the Ni_3S_2@NiMo-LDH-150 samples (Figure 3e,f).

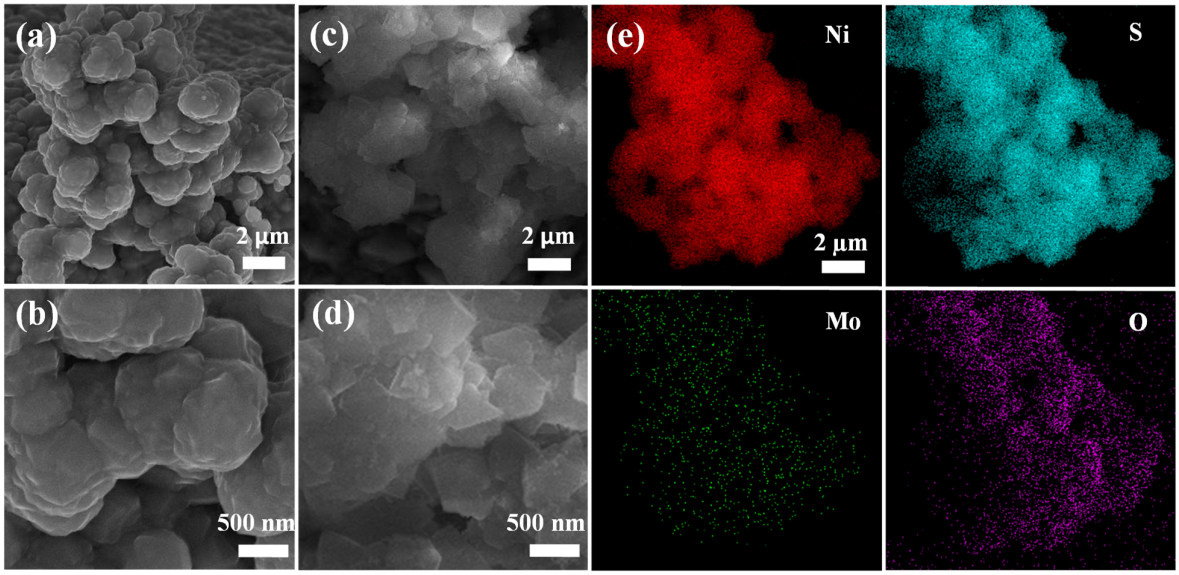

Figure 3. Morphology characterization. (**a**,**b**) SEM image of Ni_3S_2 nanospheres; (**c**,**d**) SEM image of Ni_3S_2@NiMo-LDH-150 sample; (**e**) EDS element mappings of Ni_3S_2@NiMo-LDH-150 product.

Then, the electrochemical performances are studied in a three-electrode system. Figure 4a presents the CV curves of the several electrode materials at 50 mV s^{-1}. The Ni_3S_2@NiMo-LDH-150 sample possesses the highest storage capacity. The correspond-

ing GCD curves (Figure 4b) reflect that the longer discharge duration indicates that the Ni_3S_2@NiMo-LDH-150 electrode material possesses a larger capacitance. Compared with the Ni_3S_2 product, the enhanced electrochemical performance of the Ni_3S_2@NiMo-LDH-150 sample is owing to the synergy between the two materials. Figure 4c shows the CV curves of the Ni_3S_2@NiMo-LDH-150 sample. The CV shape of the electrode hardly changes even at 50 mV s^{-1}, which possesses excellent structural stability. The redox reaction associated with Ni_3S_2@NiMo-LDH-150 is represented by the following equation [34,35]:

$$Ni_3S_2 + 3OH^- \leftrightarrow Ni_3S_2(OH)_3 + 3e^- \quad (7)$$

$$Ni(OH)_2 + OH^- \leftrightarrow NiOOH + H_2O + e^- \quad (8)$$

$$Mo(OH)_4 + 2OH^- \leftrightarrow MoO_3 + 3H_2O + 2e^- \quad (9)$$

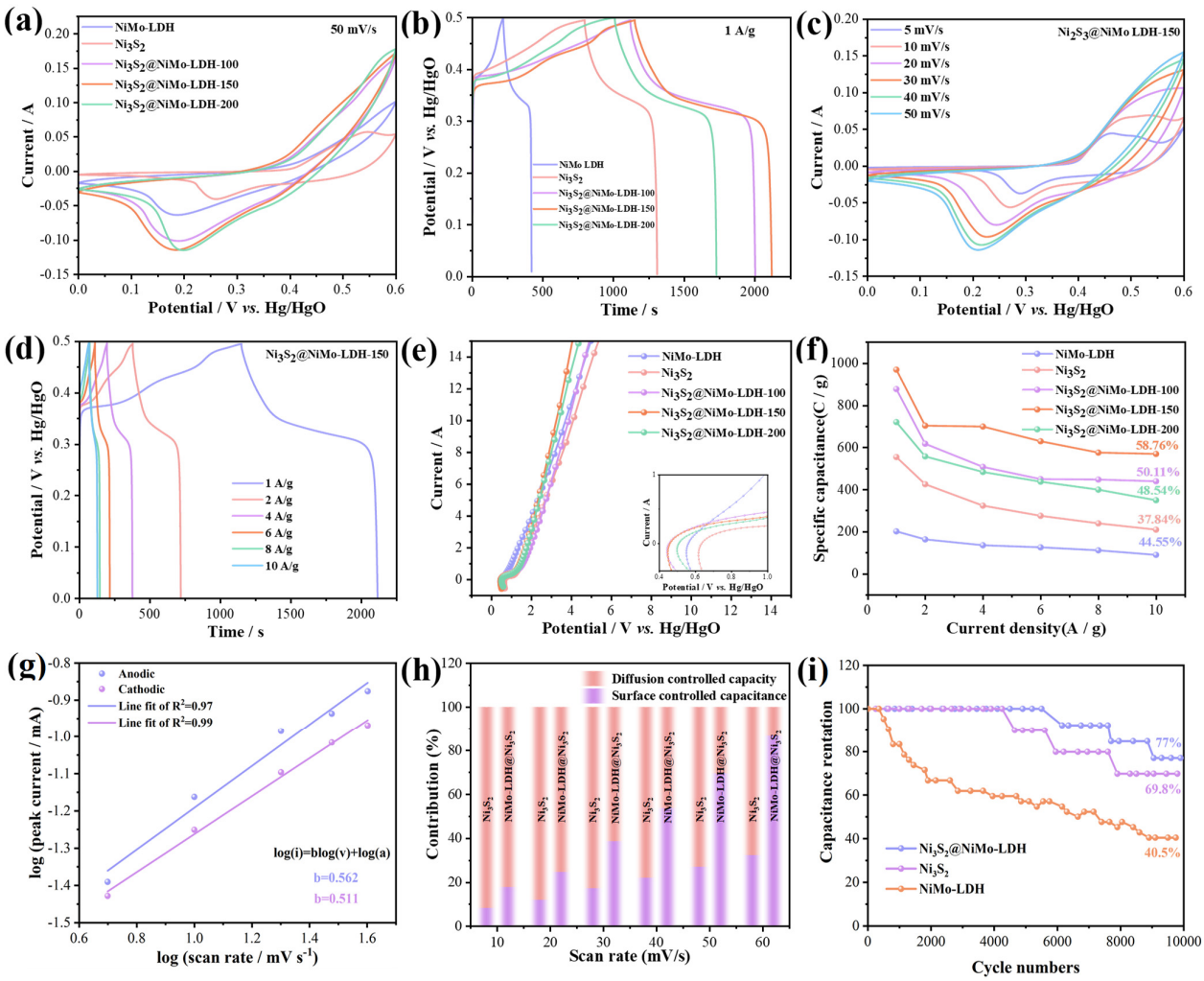

Figure 4. Electrochemical performance of the electrode materials. (**a**) CV curves; (**b**) GCD curves; (**c**) CV curves of Ni_3S_2@NiMo-LDH-150 sample at different scan rates; (**d**) GCD curves of Ni_3S_2@NiMo-LDH-150 sample at different current densities; (**e**) Nyquist plots; (**f**) specific capacitance; (**g**) b value of Ni_3S_2@NiMo-LDH-150; (**h**) capacitance contribution; (**i**) cycling performance.

From Figure 4d, the specific capacities of Ni_3S_2@NiMo-LDH-150 electrode material calculated from the GCD curves are 970, 686, 724, 630, 576, and 460 C g^{-1} at 1, 2, 4, 6, 8, and 10 A g^{-1}, respectively. EIS is an important factor used to study the conductivity of samples. Figure 4e depicts the corresponding Nyquist plots. The Ni_3S_2@NiMo-LDH-150 electrode material possesses an equivalent series resistance (R_s) value of 0.49 Ω, which is favorable to

Ni_3S_2 (0.63 Ω) and NiMo-LDH (0.56 Ω) electrode materials. Figure 4f presents the variation in the capacity of electrodes. Ni_3S_2@NiMo-LDH-150 sample is 970 C g^{-1} at 1 A g^{-1}. The specification capacitance was still 58.76% of the starting capacitance at 10 A g^{-1}. Under the same current density, Ni_3S_2 and NiMo-LDH maintain 37.84% and 44.55% capacitive retention, respectively, which indicates that the Ni_3S_2@NiMo-LDH-150 composites possess superior capacity stability. To better understand and explore the mechanism of charge storage and release in the supercapacitor Ni_3S_2@NiMo-LDH-150 electrode material. Based on the relationship between scan rate and current in the CV curve, the following equation is obtained [36]:

$$i = av^b \tag{10}$$

$$\log i = b \log v + \log a \tag{11}$$

where a and b are constants, i corresponds to peak current, ν indicates the scan rate, and the log(i) and log(ν) slopes can be computed to find the b value.

For electrode materials in which battery-type and capacitive charge storage exist, the b values obtained after fitting are usually between 0.5 and 1. Figure 4g depicts the curves obtained after fitting for the anodic and cathodic peaks, corresponding to b-values of about 0.562 and 0.511, respectively. This shows that the dominant behavior of the energy storage of this electrode material is battery-type charge storage controlled by diffusion. The contribution of capacitance is further differentiated by the following equation [37]:

$$i(V) = k_1V + k_2V^{1/2} \tag{12}$$

where i, k_1, k_2, and ν denote current, constant, constant, and scan rate, respectively.

From Figure 4h, it is observed that the capacity contributed by diffusion control to the total capacity contribution of the sample decreases with the increase in scanning rate, and the capacity contributed by surface control increases gradually. Figure 4i shows cycling curves for each electrode material at 5 A g^{-1}. It has been discovered that the Ni_3S_2@NiMo-LDH-150 sample keeps a retention rate of 77% after 10,000 cycles, which is better than other electrode materials. It demonstrates that the structure of nanosheet-coated microspheres is more stable than that of single materials. A comparison of the cycling stability of electrodes is illustrated in Table 1.

Table 1. Comparison of the cycling stability of electrode materials.

Electrode Materials	Current Density (A g^{-1})	Number of Cycles	Retention Rate (%)
Ni_3S_2@NiMo-LDH	5	10,000	77%
Ni_3S_2	5	10,000	69.8%
NiMo-LDH	5	10,000	40.5%
Ni_3S_2@NiMo-LDH//AC (25 °C)	2	10,000	84%
Ni_3S_2@NiMo-LDH//AC (0 °C)	2	2000	100%

To assess the composite in practical applications, a Ni_3S_2@NiMo-LDH-150//AC ASC device is fabricated. From Figure 5a, the voltage windows are found to be −1.0 to 0 V and 0 to 0.6 V for the Ni_3S_2@NiMo-LDH-150 and AC electrodes, respectively. Figure 5b indicates that CV curves retain a shape, demonstrating its fast charging and discharging capability. The GCD curve (Figure 5c) of the device delivers specific capacities of 102.5, 83.9, 67.4, 57, 48.4, and 42 C g^{-1} at 0.5, 1, 2, 3, 4, and 5 A g^{-1}, respectively. Figure 5d illustrates the Nyquist plot of an assembled supercapacitor device. The data show that R_s is 0.9, R_{ct} is 1.35, and CPE-P is 0.77. After six EIS measurements, the standardized deviations are computed to be R_s (AVG = 0.898, R.S.D. = 0.92%), R_{ct} (AVG = 1.37, R.S.D. = 4.74%), and CPE-P (AVG = 0.767, R.S.D. = 0.88%). The calculation reveals no significant range fluctuations in the samples, and the illustration presents the corresponding equivalent circuit. In Figure 5e, the electrochemical properties are visually assessed by means of the enclosed

area using some of the parameters in the picture. The integral area of the Ni_3S_2@NiMo-LDH-150 product under the curve is larger than that of other reports (Table 2) [38–41]. This demonstrates the dominance of the devices we assemble compared to other devices. As seen in Figure 5f, cycling stability is an important indicator of supercapacitors' performance. The device encounters excellent cycling performance, retaining 84% of its original capacitance and maintaining 97% coulombic efficiency throughout 10,000 cycles at 2 A g^{-1}.

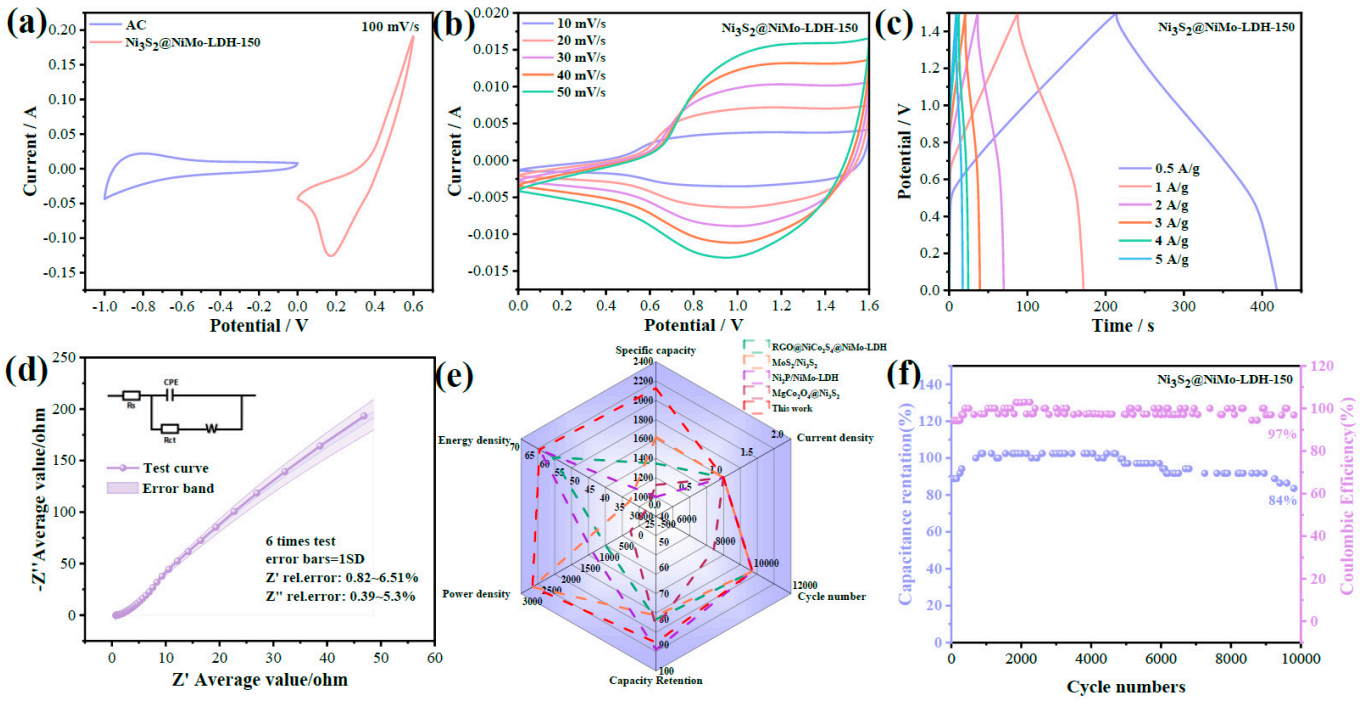

Figure 5. Electrochemical performance of the asymmetric device. (**a**) CV curves of Ni_3S_2@NiMo-LDH-150 and active carbon; (**b**) CV curves with different scan rates; (**c**) GCD curves; (**d**) Nyquist plots; (**e**) radar plots; (**f**) cycling performance.

Table 2. Electrochemical performance of the electrode materials.

Composite Materials	Specific Capacity (1 A/g)	Energy Density (W h kg^{-1})	Power Density (W kg^{-1})	Cycle Number	Capacity Retention Rate	Ref.
RGO@$NiCo_2S_4$@NiMo-LDH//AC	1346 F g^{-1}	59.38	808.19	10,000	80%	[36]
MoS_2/Ni_3S_2//AC	1001 F g^{-1}	33.75	2700	10,000	78.5%	[37]
Ni_2P/NiMo-LDH//AC	1620 F g^{-1}	63.7	1138.3	10,000	91.7%	[38]
$MgCo_2O_4$ @Ni_3S_2//AC	1123 F g^{-1}	28.37	159.6	8000	82.9%	[39]
Ni_3S_2@NiMo-LDH//AC	1940 F g^{-1}	63.8	2701.6	10,000	89%	This work

Finally, we explored the mechanical stability and practical application of the device under various conditions. Figure 6a shows the photos of the device under different bending angles. Figure 6b–d illustrate that the CV curves of the device under repeated bending at various angles are virtually unchanged, indicating that it possesses excellent flexibility and mechanical stability. At 0 °C, Figure 6e represents that the cycling stability of the device is virtually undiminished after 2000 cycles at 2 A g^{-1}. The inset indicates that three devices that are connected can light up a blue LED lamp for 9 min, which provides powerful support for real-world applications.

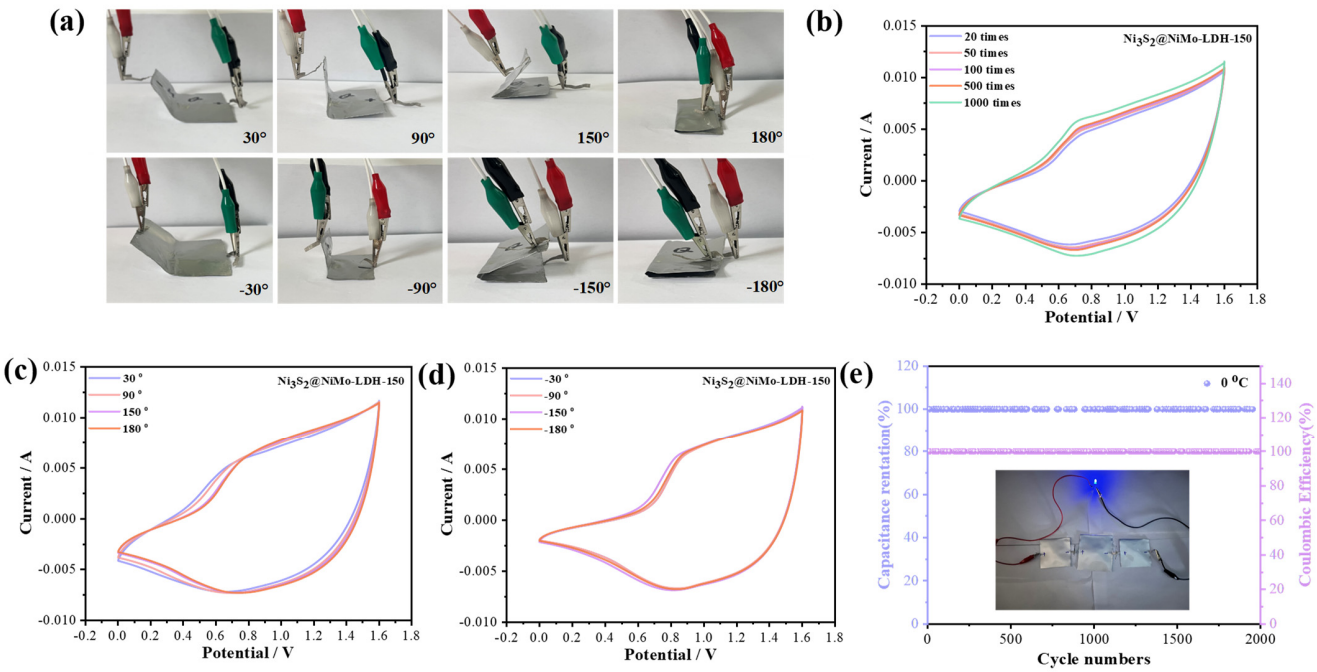

Figure 6. Electrochemical performance of the asymmetric device. (**a**) Digital photographs of the folded device; (**b**) CV curves with various bending times; (**c**,**d**) CV curves with various bending angles; (**e**) low-temperature cycle performance.

4. Conclusions

In conclusion, NiMo-LDH nanosheet-decorated Ni_3S_2 microspheres are prepared via a combination of hydrothermal and electrodeposition routes. Compared with Ni_3S_2 and NiMo-LDH single samples, Ni_3S_2@NiMo-LDH-150 hybrids are characterized by a large specific surface area, high conductivity, and strong electrochemical activity. Therefore, the Ni_3S_2@NiMo-LDH-150 product provides excellent electrochemical performance. An assembled ASC provides high energy and power densities and shows great low-temperature stability and flexibility via low-temperature cycling and multi-angle bending tests. The experiments demonstrate that the reasonable design of the Ni_3S_2@NiMo-LDH-150 composite makes up for the deficiency of a single material and indicates excellent application potential in supercapacitors.

Author Contributions: Q.H.: methodology, conceptualization, software, data curation, writing—original draft preparation, visualization, and software. X.W.: supervision and writing—reviewing and editing. All authors have read and agreed to the published version of the manuscript.

Funding: This project was supported by the Natural Science Foundation of China (no. 52172218).

Data Availability Statement: Data will be made available on request.

Conflicts of Interest: The authors declare no conflicts of interest.

References

1. Rani, B.J.; Sivanantham, A.; Cho, I.S. Nanostructured Spinel Manganates and Their Composites for Electrochemical Energy Conversion and Storage. *Adv. Funct. Mater.* **2023**, *33*, 2303002. [CrossRef]
2. Zhang, J.J.; Wu, X. Dual-ion carrier storage through Mg^{2+} addition for high-energy and long-life zinc-ion hybrid capacitor. *Int. J. Miner. Metall. Mater.* **2024**, *31*, 179–185. [CrossRef]
3. Lu, C.; Tu, C.; Yang, Y.; Ma, Y.; Zhu, M. Construction of Fe_3O_4@Fe_2P Heterostructures as Electrode Materials for Supercapacitors. *Batteries* **2023**, *9*, 326. [CrossRef]
4. Zhu, S.; Sheng, J.; Chen, Y.; Ni, J.F.; Li, Y. Carbon nanotubes for flexible batteries: Recent progress and future perspective. *Natl. Sci. Rev.* **2021**, *8*, nwaa261. [CrossRef] [PubMed]
5. Liu, Y.; Wu, X. High durable aqueous zinc ion batteries by synergistic effect of V_6O_{13}/VO_2 electrode materials. *J. Energy Chem.* **2023**, *87*, 334–341. [CrossRef]

6. Shah, S.S.; Aziz, M.A.; Al Marzooqi, M.; Khan, A.Z.; Yamani, Z.H. Enhanced light-responsive supercapacitor utilizing $BiVO_4$ and date leaves-derived carbon: A leap towards sustainable energy harvesting and storage. *J. Power Sources* **2024**, *602*, 234334. [CrossRef]
7. Liu, R.X.; Liu, W.K.; Chen, J.C.; Bian, X.L.; Fan, K.Q.; Zhao, J.H.; Zhang, X.J. Acrylate Copolymer-Reinforced Hydrogel Electrolyte for Strain Sensors and Flexible Supercapacitors. *Batteries* **2023**, *9*, 304. [CrossRef]
8. Khan, J.; Shakeel, N.; Alam, S.; Alam, F.; Dahshan, A. Sulfurization of Electrode Material: A Promising Window for Supercapacitor Technology. *Batter. Supercaps* **2024**, *7*, e202300366. [CrossRef]
9. Wang, S.; Ma, J.X.; Shi, X.Y.; Zhu, Y.Y.; Wu, Z.S. Recent status and future perspectives of ultracompact and customizable micro-supercapacitors. *Nano Res. Energy* **2022**, *1*, e9120018. [CrossRef]
10. Zhao, Y.; Guo, J.; Liu, A.; Ma, T. 2D heterostructure comprised of Ni_3S_2/d-Ti_3C_2 supported on Ni foam as binder-free electrode for hybrid supercapacitor. *J. Alloy. Compd.* **2020**, *814*, 152271. [CrossRef]
11. Wang, X.W.; Sun, Y.C.; Zhang, W.C.; Wu, X. Flexible $CuCo_2O_4$@Ni-Co-S hybrids as electrode materials for high-performance energy storage devices. *Chin. Chem. Lett.* **2023**, *34*, 107593. [CrossRef]
12. Zhu, S.; Li, Y.T.; Zhu, H.Y.; Ni, J.F.; Li, Y. Pencil-Drawing Skin-Mountable Micro-Supercapacitors. *Small* **2019**, *15*, 1804037. [CrossRef]
13. Ali, Z.; Iqbal, M.Z.; Hegazy, H.H. Recent advancements in redox-active transition metal sulfides as battery-grade electrode materials for hybrid supercapacitors. *J. Energy Storage* **2023**, *73*, 108857. [CrossRef]
14. Li, T.S.; Zhao, Z.F.; Su, Z.H.; Lin, S.Y.; Sun, R.; Shang, Y.C. One-step electrodeposited Ni_3S_2/Co_9S_8/NiS composite on Ni foam as high-performance electrode for supercapacitors. *Dalton Trans.* **2023**, *52*, 6823–6830. [CrossRef] [PubMed]
15. Li, J.P.; Liu, X.P.; Zhao, H.Y.; Yang, X.B.; Xiao, S.Y.; Liu, N.L.; Zhao, N.N.; Cao, Y.Y.; Yu, X.J.; Li, X.F. Dual-Phase engineering of Ni_3S_2/NiCo-MOF nanocomposites for enhanced ion storage and electron migration. *Chem. Eng. J.* **2024**, *489*, 151069. [CrossRef]
16. Wu, B.X.; Qian, H.; Nie, Z.W.; Luo, Z.P.; Wu, Z.X.; Liu, P.; He, H.; Wu, J.H.; Chen, S.G.; Zhang, F.F. Ni_3S_2 nanorods growing directly on Ni foam for all-solid-state asymmetric supercapacitor and efficient overall water splitting. *J. Energy Chem.* **2020**, *46*, 178–186. [CrossRef]
17. Guo, Z.C.; Mu, J.P.; Wang, J.P.; Mu, J.B.; Che, H.W.; Li, F.; Yang, H.; He, L.X.; Wei, F.F. Rational fabrication and optimized design of hierarchical Ni_3S_2-MOF electrodes for enhanced electrochemical energy storage. *J. Energy Storage* **2023**, *70*, 108019. [CrossRef]
18. Wang, W.Y.; Yang, C.; Han, D.T.; Yu, S.J.; Qi, W.T.; Ling, R.; Liu, G.Q. Ni_3S_2/Ni_2O_3 heterojunction anchored on N-doped carbon nanosheet aerogels for dual-ion hybrid supercapacitors. *J. Colloid Interface Sci.* **2024**, *654*, 709–718. [CrossRef]
19. Wang, Y.T.; He, X.F.; He, G.Y.; Meng, C.; Chen, X.M.; Li, F.T. A critical review on nickel sulfide-based electrode materials for supercapacitors. *Crit. Rev. Solid State Mat. Sci.* **2023**, *48*, 502–518. [CrossRef]
20. Li, X.; Ren, J.; Sridhar, D.; Xu, B.B.; Algadi, H.; El-Bahy, Z.M.; Ma, Y.; Li, T.; Guo, Z. Progress of layered double hydroxide-based materials for supercapacitors. *Mat. Chem. Front.* **2023**, *7*, 1520–1561. [CrossRef]
21. Wang, M.D.; Liu, X.Y.; Wu, X. Realizing efficient electrochemical overall water electrolysis through hierarchical CoP@NiCo-LDH nanohybrids. *Nano Energy* **2023**, *114*, 108681. [CrossRef]
22. Wang, Y.; Zhang, M.; Liu, Y.; Zheng, Z.; Liu, B.; Chen, M.; Guan, G.; Yan, K. Recent advances on transition-metal-based layered double hydroxides nanosheets for electrocatalytic energy conversion. *Adv. Sci.* **2023**, *10*, 2207519. [CrossRef] [PubMed]
23. Wang, G.; He, L.; Guo, Z.; Li, M. Ternary metal layered hydroxides: As promising electrode materials for supercapacitors. *J. Energy Storage* **2023**, *72*, 108544. [CrossRef]
24. Wang, Z.; Liu, Y.; Cheng, W.; Huang, W.; Sun, Y.; Cui, L.; Xu, J.; Liu, J. Nanoflower-like Ag adhered NiMo$(OH)_x$ composite arrays on nickel foam for high-performance supercapacitor. *J. Energy Storage* **2024**, *81*, 110246. [CrossRef]
25. Huang, B.J.; Yao, D.C.; Yuan, J.J.; Tao, Y.R.; Yin, Y.X.; He, G.Y.; Chen, H.Q. Hydrangea-like $NiMoO_4$-Ag/rGO as Battery-type electrode for hybrid supercapacitors with superior stability. *J. Colloid Interface Sci.* **2022**, *606*, 1652–1661. [CrossRef] [PubMed]
26. Liu, J.X.; Zhao, S.Q.; Wu, X. Flexible electrochemical capacitor based NiMoSSe electrode material with superior cycling and structural stability. *Chin. Chem. Lett.* **2024**, *35*, 109059. [CrossRef]
27. Bandyopadhyay, P.; Saeed, G.; Kim, N.H.; Lee, J.H. Zinc-nickel-cobalt oxide@$NiMoO_4$ core-shell nanowire/nanosheet arrays for solid state asymmetric supercapacitors. *Chem. Eng. J.* **2020**, *384*, 123357. [CrossRef]
28. Liang, J.Y.; Qin, S.M.; Luo, S.; Pan, D.; Xu, P.F.; Li, J. Honeycomb porous heterostructures of NiMo layered double hydroxide nanosheets anchored on CoNi metal–organic framework nano-blocks as electrodes for asymmetric supercapacitors. *J. Colloid Interface Sci.* **2024**, *653*, 504–516. [CrossRef]
29. Qian, H.; Wu, B.X.; Nie, Z.W.; Liu, T.T.; Liu, P.; He, H.; Wu, J.H.; Chen, Z.Y.; Chen, S.G. A flexible Ni_3S_2/Ni@CC electrode for high-performance battery-like supercapacitor and efficient oxygen evolution reaction. *Chem. Eng. J.* **2021**, *420*, 127646. [CrossRef]
30. Shi, R.D.; Yang, J.S.; Zhou, G.B. High-index-faceted and electron density-optimized Ni_3S_2 in hierarchical $NiWO_4$-Ni_3S_2@NiO/NF nanofibers for robust alkaline electrocatalytic hydrogen evolution. *Chem. Eng. J.* **2023**, *457*, 141188. [CrossRef]
31. Liu, S.; He, S.W.; Xiang, Y.H.; Peng, X.C.; Xiong, L.Z.; Wu, J.H. Zn-Co-Mo-rGO ultra-thin nanosheets arrays-based electrode materials for asymmetric supercapacitor. *Batteries* **2023**, *9*, 158. [CrossRef]
32. Duan, C.; Wang, L.; Liu, J.; Qu, Y.; Gao, J.; Yang, Y.; Wang, B.; Li, J.; Zheng, L.; Li, M.; et al. 3D Carbon Electrode with Hierarchical Nanostructure Based on NiCoP Core-Layered Double Hydroxide Shell for Supercapacitors and Hydrogen Evolution. *ChemElectroChem* **2021**, *8*, 2272–2281. [CrossRef]

33. Wang, M.D.; Liu, X.Y.; Sun, Y.C.; Wu, X. High-efficiency NiCo layered double hydroxide electrocatalyst. *New J. Chem.* **2022**, *38*, 18535–18542. [CrossRef]
34. Yu, G.; Zhou, J.; Chen, Q.; Huang, Z.; Tao, K.; Han, L. Controllable fabricate hierarchical $CoMoO_3$@Co_9S_8/Ni_3S_2 core-shell arrays for high-performance hybrid supercapacitor. *Mater. Today Chem.* **2023**, *30*, 101601. [CrossRef]
35. Wang, S.; Hu, C.H.; Wang, J.H.; Xie, M.Z.; Wu, S.Y.; Zhao, L.H.; Gong, J.X.; Dai, Y.T. Sugar gourd-like NiCo layered double hydroxide@$NiMoO_4$ hierarchical core-shell material for high-performance asymmetric supercapacitors. *J. Energy Storage* **2023**, *73*, 109034. [CrossRef]
36. Xiong, Y.; Yu, F.; Arnold, S.; Wang, L.; Presser, V.; Ren, Y.; Ma, J. Three-dimensional cobalt hydroxide hollow cube/vertical nanosheets with high desalination capacity and long-term performance stability in capacitive deionization. *Research* **2021**, *2021*, 9754145. [PubMed]
37. Shi, M.M.; Zhao, M.S.; Jiao, L.D.; Su, Z.; Li, M.; Song, X.P. Novel Mo-doped nickel sulfide thin sheets decorated with Ni–Co layered double hydroxide sheets as an advanced electrode for aqueous asymmetric super-capacitor battery. *J. Power Sources* **2021**, *509*, 230333. [CrossRef]
38. Cheng, C.; Zou, Y.J.; Xu, F.; Xiang, C.L.; Sui, Q.L.; Zhang, J.; Sun, L.X.; Chen, Z.M. Ultrathin graphene@$NiCo_2S_4$@Ni-Mo layered double hydroxide with a 3D hierarchical flowers structure as a high performance positive electrode for hybrid supercapacitor. *J. Energy Storage* **2022**, *52*, 105049. [CrossRef]
39. Liu, J.X.; Wu, X. Nanosheet-assembled MoS_2/Ni_3S_2 microspheres for flexible energy storage devices. *J. Solid State Electrochem.* **2023**, *27*, 2571–2577. [CrossRef]
40. Jiang, D.Y.; Wang, Y.Q.; Du, C.; Xie, M.J.; Chen, J.; Zhang, Y.; Wan, L. Heterostructured Ni_2P/NiMo-layered double hydroxide nanoarrays with enriched redox active sites for supercapacitors. *J. Alloy. Compd.* **2024**, *970*, 172685. [CrossRef]
41. He, W.X.; Pang, M.J.; Jiang, S.; Yang, H.; Wang, R.W.; Li, N.; Pan, Q.L.; Li, J.W.; Zhao, J.G. Binder-free $MgCo_2O_4$@Ni_3S_2 core-shell-like composites as advanced battery materials for asymmetric supercapacitors. *Synth. Met.* **2022**, *285*, 117021. [CrossRef]